Controlled Synthesis of Pd–Pt Alloy Hollow Nanostructures with Enhanced Catalytic Activities for Oxygen Reduction

Jong Wook Hong,[†] Shin Wook Kang,[†] Bu-Seo Choi,[†] Dongheun Kim,[‡] Sang Bok Lee,[‡,§] and Sang Woo Han[†,*]

[†]Department of Chemistry and KI for the NanoCentury and [‡]Graduate School of Nanoscience and Technology (WCU), KAIST, Daejeon 305-701, Korea, and
[§]Department of Chemistry and Biochemistry, University of Maryland, College Park, Maryland 20742, United States

ABSTRACT Pd–Pt alloy nanocrystals (NCs) with hollow structures such as nanocages with porous walls and dendritic hollow structures and Pd@Pt core–shell dendritic NCs could be selectively synthesized by a galvanic replacement method with uniform Pd octahedral and cubic NCs as sacrificial templates. Fine control over the degree of galvanic replacement of Pd with Pt allowed the production of Pd–Pt NCs with distinctly different morphologies. The synthesized hollow NCs exhibited considerably enhanced oxygen reduction activities compared to those of Pd@Pt core–shell NCs and a commercial Pt/C catalyst, and their electrocatalytic activities were highly dependent on their morphologies. The Pd–Pt nanocages prepared from octahedral Pd NC templates exhibited the largest improvement in catalytic performance. We expect that the present work will provide a promising strategy for the development of efficient oxygen reduction electrocatalysts and can also be extended to the preparation of other hybrid or hetero-nanostructures with desirable morphologies and functions.

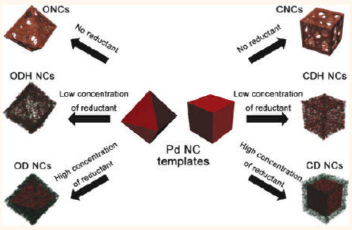

KEYWORDS: electrocatalysis · hollow nanocrystals · oxygen reduction · palladium · platinum

Among various alternative energy sources, proton exchange membrane fuel cells (PEMFCs) have attracted considerable attention due to their high efficiency, low operation temperature, and environmentally benign products.[1–3] However, for the commercialization of PEMFCs, the sluggish kinetics of the oxygen reduction reaction (ORR) at the cathode must be overcome.[4–6] To address this issue, a great deal of efforts have been devoted to improving the ORR activity with Pt-based catalysts because Pt is the most effective catalytic material toward ORR in PEMFCs.[7,8] A number of previous works showed that the electrocatalytic activities of Pt could be improved by tailoring the shape of Pt nanostructures.[9–12] For example, Pt nanowires and nanocubes exhibited higher ORR performances than spherical Pt nanoparticles.[9,10] Noticeably, Adzic and co-workers reported that Pt hollow nanocrystals (NCs) are the most suitable catalyst to enhance sustainable ORR activity, with this structure increasing both durability and Pt mass activity for oxygen reduction in acid fuel cells.[11] On the other hand, the use of Pt-based bimetallic NCs (Pt-M NCs, where M = Pd, Co, Ni, Fe, Au, Cu, *etc.*) in place of pure Pt as electrocatalysts is also an effective strategy to increase the specific activity and mass activity of Pt catalysts.[13–22] The introduction of other metal compositions not only decreases the amount of Pt required in electrocatalysis but also modifies the crystallographic and electronic structures of Pt, which can optimize the binding energy between Pt and oxygen.[23] In particular, Pd is known for its capacity to enhance the ORR activity and durability of Pt.[24–26] On the basis of this background, Pd–Pt bimetallic NCs with hollow structures are considered to be a highly promising candidate for efficient ORR electrocatalysts. However, the controlled synthesis of Pd–Pt hollow NCs with a range of morphologies and their electrocatalytic properties toward ORR have been rarely studied to date.

The galvanic replacement reaction has been widely applied to synthesize NCs with hollow features.[27] To exploit galvanic replacement in the formation of a hollow nanostructure, the reduction potential of a sacrificial metallic template should be sufficiently lower than that of the metal composing the final hollow structure. In this regard, Ag NCs have frequently been used as sacrificial templates to produce Pd and/or Pt hollow nanostructures owing to the

* Address correspondence to sangwoohan@kaist.ac.kr.

Received for review December 2, 2011 and accepted February 23, 2012.

10.1021/nn2046828

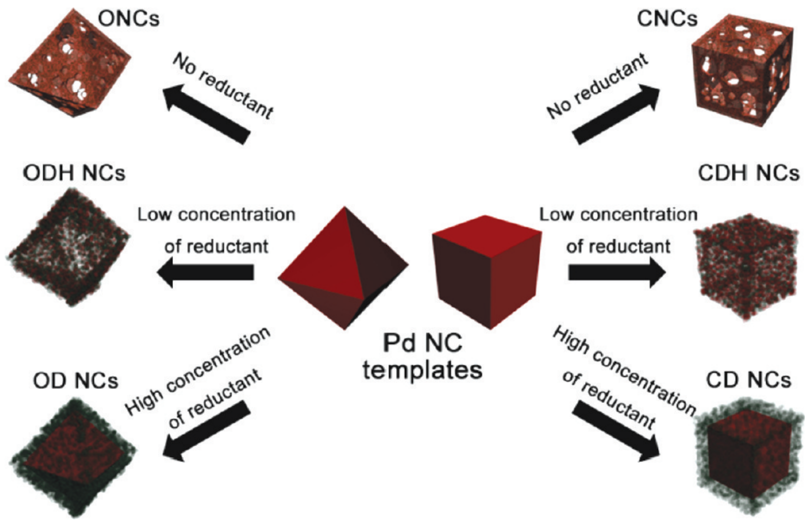

Scheme 1. Schematic illustration for the synthetic parameters to produce various types of Pd–Pt bimetallic NCs from Pd NC templates.

much lower reduction potential of Ag relative to those of Pd and Pt.[28−31] In the present work, we used Pd NCs with well-defined morphologies, such as octahedral and cubic structures, as sacrificial templates to generate Pd–Pt NCs with hollow interiors. Interestingly, maneuvering the degree of galvanic replacement of Pd with Pt yielded hollow Pd–Pt alloy NCs with distinctly different morphologies, that is, nanocages with porous walls and dendritic hollow structures of which the hollow interiors were closely related to the original Pd NC templates. The synthesized hollow NCs exhibited higher ORR activities than those of Pd@Pt core–shell NCs without a hollow feature, and their electrocatalytic activities were highly dependent on their morphologies.

RESULTS AND DISCUSSION

To generate Pd–Pt hollow NCs, uniform octahedral and cubic Pd NCs were first prepared in aqueous solutions using cetyltrimethylammonium chloride (CTAC) and ascorbic acid (AA) as a surfactant and reductant, respectively (see Methods section). The average edge lengths of octahedral and cubic Pd NCs were adjusted to approximately the same value of 25 nm (Figure S1 in the Supporting Information (SI)). These Pd NCs were then used as seeds for the formation of Pd–Pt bimetallic hollow NCs. We successfully synthesized four different types of Pd–Pt bimetallic NCs with hollow structures: octahedral nanocages (ONCs), cubic nanocages (CNCs), octahedral dendritic hollow (ODH) NCs, and cubic dendritic hollow (CDH) NCs. For comparison, we also prepared two types of dendritic Pd@Pt core–shell NCs without a hollow interior: octahedral dendritic (OD) NCs and cubic dendritic (CD) NCs. Since the catalytic functions of NCs are influenced by the surfactant molecules, all of the Pd–Pt bimetallic NCs were synthesized in the presence of the same surfactant, CTAC, for precise comparison of inherent ORR properties between different NCs. Scheme 1 summarizes the general synthetic routes for the preparation of Pd–Pt bimetallic NCs with different morphologies. The ONCs and CNCs with porous walls and hollow interiors were prepared *via* the galvanic replacement reaction with a Pt precursor, K_2PtCl_4, for 24 h using octahedral and cubic Pd NC templates, respectively, in the absence of AA. On the other hand, the galvanic replacement reaction for 16 h in the presence of AA (final concentration of 2.5 mM) as a reductant produced Pd–Pt NCs with hollow interiors and numerous dendritic branches. The shapes of hollow interiors of these four types of NCs followed those of their corresponding templates. When a higher amount of AA (10 mM) was used, dendritic Pd@Pt core–shell NCs with no hollow interiors were formed within 3 h.

The as-prepared Pd–Pt bimetallic NCs were characterized by transmission electron microscopy (TEM) (Figure 1) and scanning electron microscopy (SEM) measurements (Figure S2 in SI). The TEM and SEM images clearly show the formation of uniform Pd–Pt NCs with well-defined morphologies. As shown in Figure 1a–d, the ONCs, CNCs, ODH NCs, and CDH NCs have hollow interiors in common. The ONCs and CNCs have porous walls with an average thickness of ~1.5 nm (Figure 1a,b), whereas ODH and CDH NCs have numerous dendritic branches on their surfaces (Figure 1c,d). In comparison with ODH and CDH NCs, OD and CD NCs have similar dendritic branches, but their central parts, unlike ODH and CDH NCs, are composed of Pd seeds instead of empty space (Figure 1e,f). The average lengths of the dendritic branches of the ODH, CDH, OD, and CD NCs are 8.5, 8.2, 7.9, and 8.1 nm, respectively. The hollow interiors or Pd cores of the prepared NCs have the same shapes as and similar sizes (~25 nm) to the Pd NC templates.

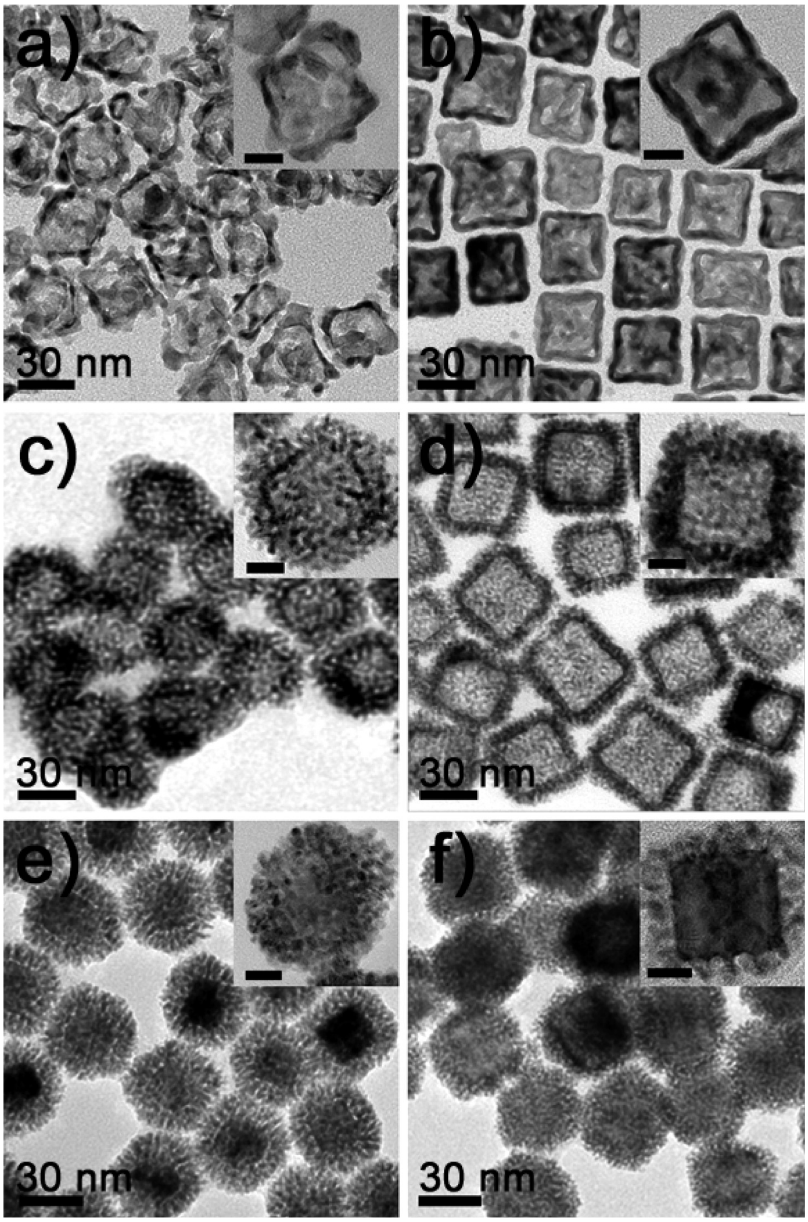

Figure 1. TEM images of (a) ONCs, (b) CNCs, (c) ODH NCs, (d) CDH NCs, (e) OD NCs, and (f) CD NCs. High-magnification TEM images are shown in each inset. Scale bars in the insets indicate 10 nm.

The high-angle annular dark-field scanning TEM (HAADF-STEM) images of the Pd–Pt bimetallic NCs further confirmed their structural characteristics (Figure 2), and corresponding energy-dispersive X-ray spectroscopy (EDS) mapping (Figure 2) and cross-sectional compositional line profiles (Figure 3) clearly revealed their compositional structures. Figure 2a,b and Figure 3a,b show that the thin porous walls of the ONCs and CNCs comprise a Pd–Pt alloy. For the ODH and CDH NCs, Pd–Pt alloy features were indentified at their dendritic branches as well as at their walls (Figure 2c,d and Figure 3c,d), whereas the dendritic shells and cores of the OD and CD NCs were formed only by Pt and Pd, respectively (Figure 2e,f and Figure 3e,f). Inductively coupled plasma atomic emission spectroscopy (ICP-AES) exhibited that the actual composition ratios of Pt in the synthesized NCs were 62.9, 61.5, 69.3, 68.7, 52.6, and 49.6% for the ONCs, CNCs, ODH NCs, CDH NCs, OD NCs, and CD NCs, respectively. The surface compositions of Pt in the ONCs, CNCs, ODH NCs, and CDH NCs were maesured to be 80.8, 80.3, 84.8, and 81.7%, respectively, by Auger electron spectroscopy, also indicating the alloy nature of their surfaces with similar compostions.

We further characterized the Pd–Pt bimetallic NCs by high-resolution TEM (HRTEM) to obtain more detailed information on the growth manner and surface features of the NCs, as shown in Figure 4. The corresponding fast Fourier transform (FFT) patterns are also shown in the insets of HRTEM images. The *d* spacing for

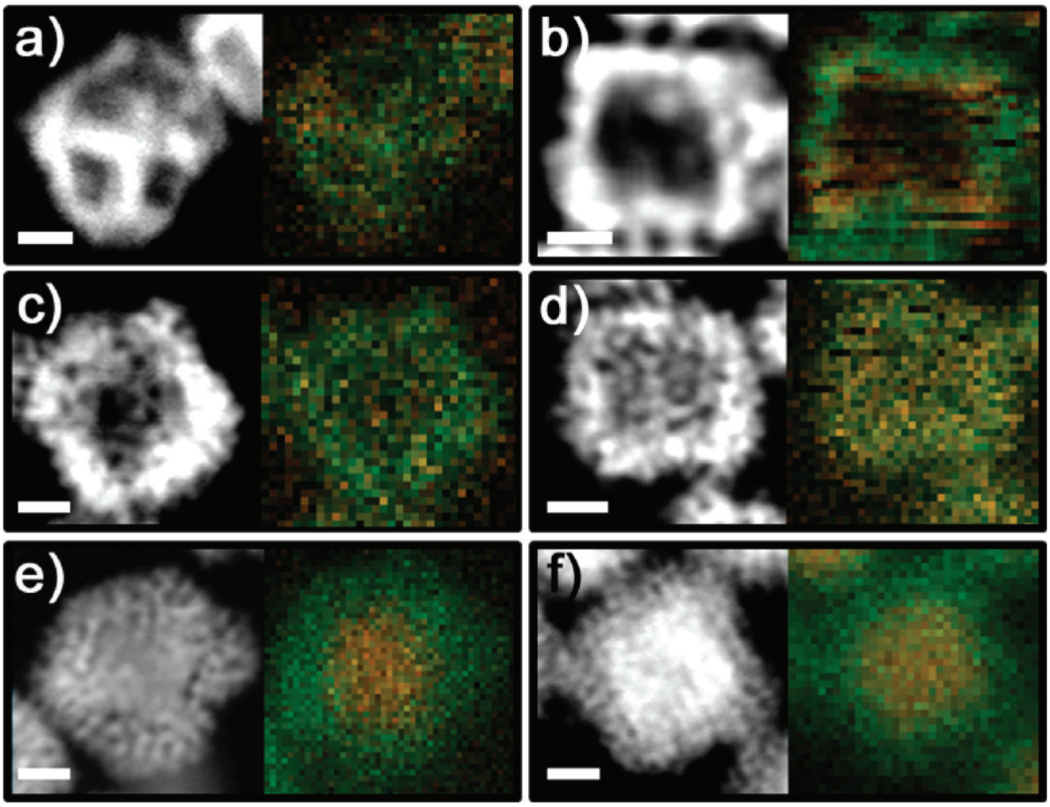

Figure 2. (Left panels) HAADF-STEM images and (right panels) corresponding HAADF-STEM-EDS mapping images of a (a) ONC, (b) CNC, (c) ODH NC, (d) CDH NC, (e) OD NC, and (f) CD NC. The yellow and green colors in HAADF-STEM-EDS mapping images indicate Pd and Pt, respectively. The scale bars indicate 10 nm.

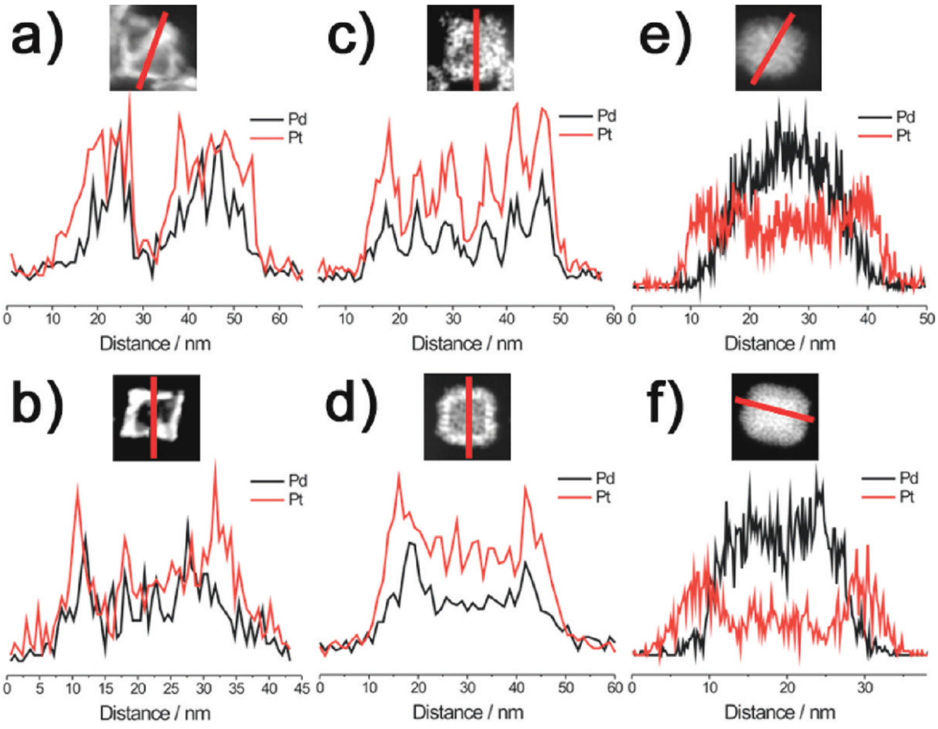

Figure 3. HAADF-STEM images and cross-sectional compositional line profiles of a (a) ONC, (b) CNC, (c) ODH NC, (d) CDH NC, (e) OD NC, and (f) CD NC. For the hollow NCs including ONC, CNC, ODH NCs, and CDH NCs, Pt traces match well with those of the Pd traces, identifying the Pd–Pt alloy structures. The compositional line profiles for OD and CD NCs clearly confirm the Pd@Pt core–shell structures.

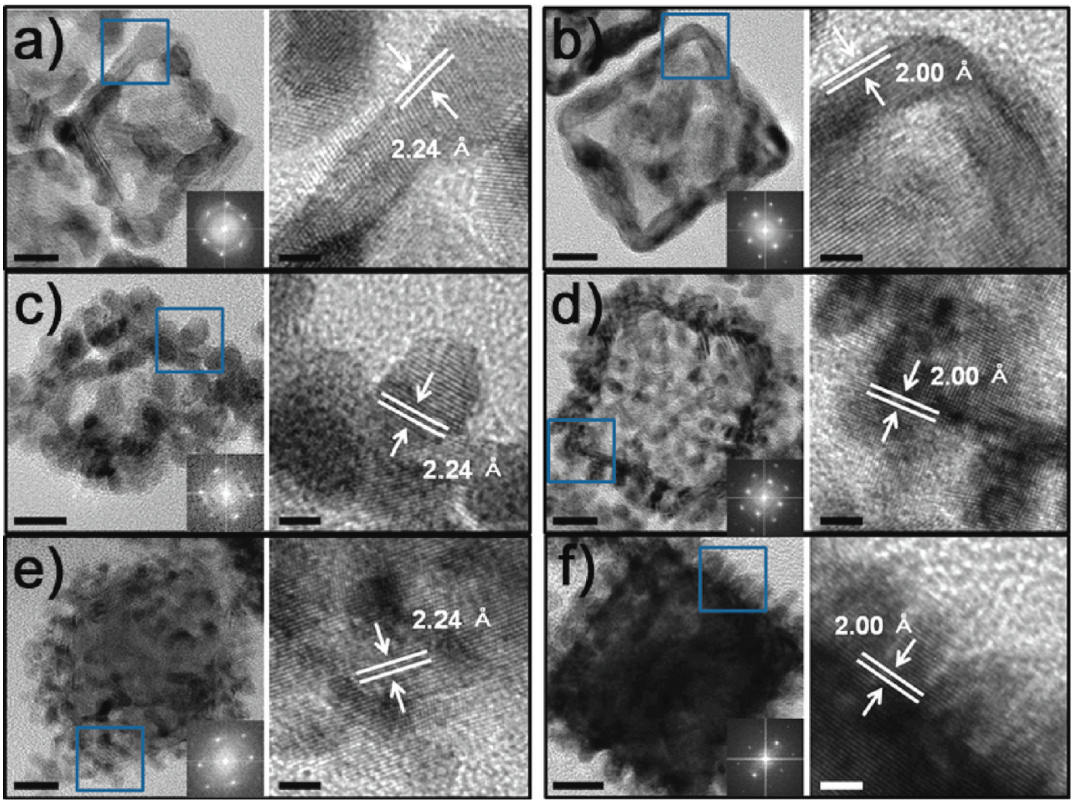

Figure 4. (Left panels) HRTEM images of a (a) ONC, (b) CNC, (c) ODH NC, (d) CDH NC, (e) OD NC, and (f) CD NC. The scale bars indicate 10 nm. Corresponding FFT patterns are shown in each inset. (Right panels) High-magnification images of the square regions in the HRTEM images shown in left panels. The scale bars indicate 2 nm.

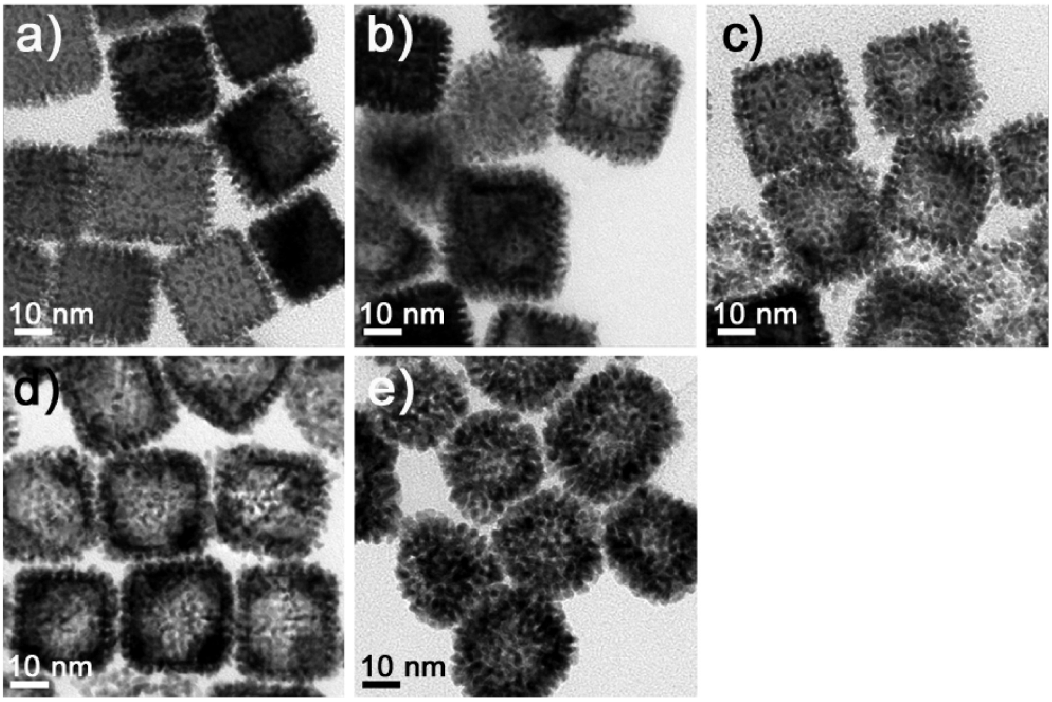

Figure 5. TEM images of CDH NCs collected at different reaction times: (a) 3, (b) 6, (c) 9, (d) 12, and (e) 16 h.

adjacent lattice fringes of the wall of the ONCs is 2.24 Å, which corresponds to that of the (111) planes of face-centered cubic (fcc) Pd, Pt, or Pd—Pt alloy (Figure 4a).[32] ODH and OD NCs also showed identical *d* spacing values (Figure 4c,e). These results indicate that the surfaces of all of the ONCs, ODH NCs, and OD NCs prepared using

{111}-faceted octahedral Pd NC templates are bound by {111} facets. On the contrary, *d* spacings of 2.00 Å between adjacent lattice fringes of CNCs, CDH NCs, and CD NCs reveal the growth of the {100}-faceted surfaces of Pd–Pt NCs from the cubic Pd NC templates enclosed by {100} facets (Figure 4b,d,f).[33] These findings definitely demonstrate that the crystallographic as well as structural characteristics of the Pd NC templates have a profound influence on the growth habit of the Pd–Pt NCs. The close correlation in crystallographic properties between the Pd–Pt NCs and Pd templates can be due to the very small lattice mismatch between Pd and Pt (0.77%).[34,35] The X-ray diffraction (XRD) patterns of the Pd–Pt NCs also show the distinct diffraction peaks from the reflections of the fcc structure of the metal (Figure S3 in SI), identifying the crystalline nature of the prepared NCs. For comparison, the XRD patterns of pristine Pd NC templates are also shown in Figure S4 in SI.

In the present work, Pd–Pt bimetallic NCs with different morphologies were obtained by adjusting the degree of galvanic replacement. When Pd NCs are used as sacrificial templates, reduction of the Pt precursors is less efficient and thus slow compared to the case where Ag NCs are employed as templates; the difference in the reduction potential between $PtCl_4^{2-}$ and Ag^+ is 0.5 V, while that between $PtCl_4^{2-}$ and $PdCl_4^{2-}$ is 0.2 V.[36] Therefore, the reductant can considerably affect the degree of galvanic replacement, such that the final morphology of the bimetallic NCs can be tuned by altering the amount of reductant. Addition of a sufficient amount of reductant into the reaction mixture, which can reduce all the Pt precursors ($PtCl_4^{2-}$), will prevent the galvanic replacement of Pd with Pt.[37,38] In relation to this, when 10 mM of AA was used as a reductant, Pt branches grown on the surface of Pd NCs with no observable galvanic replacement reaction, thus forming dendritic Pd@Pt core–shell NCs without a hollow structure (OD and CD NCs). When 2.5 mM of AA, which can reduce some portion of $PtCl_4^{2-}$, was employed, dendritic hollow NCs (ODH and CDH NCs) were generated through both Pt deposition and galvanic replacement (*vide infra*). In the absence of AA, $PtCl_4^{2-}$ could be reduced solely by the galvanic replacement reaction, and Pd–Pt alloy nanocages (ONCs and CNCs) were thereby produced.[39−41] Very recently, Xia *et al.* reported the synthesis of Pd–Pt alloy cubic nanocages using Pd nanocubes as templates and their enhanced performance for CO oxidation.[42] Contrary to our case, they found that bromide ion-induced galvanic replacement complemented with a coreduction process through the introduction of citric acid as a reductant was inevitable for the formation of the nanocages. Pd–Pt NCs with a concave structure instead of nanocages were generated without citric acid. This was attributed to the bromide ion-induced galvanic replacement selectively from the {100} facets of Pd nanocubes. As such, Pd atoms were dissolved mainly from the {100}-faceted nanocube faces and Pt atoms preferentially deposited on the {111}-faceted corners of Pd nanocubes in the absence of an additional reductant, eventually Pd–Pt concave nanocubes without a hollow feature were evolved. Furthermore, controlling the morphology of Pd–Pt nanocages by altering the shape of Pd NC templates was very difficult due to the high selectivity of bromide ion-induced galvanic replacement for the {100} facets of Pd. For instance, Pd–Pt nanocages could not be produced by using truncated octahedral Pd NCs, which were mainly enclosed by {111} facets, as sacrificial templates. These facts thus imply that our method is very simple and versatile for the synthesis of Pd–Pt hollow nanostructures with tailored morphologies.

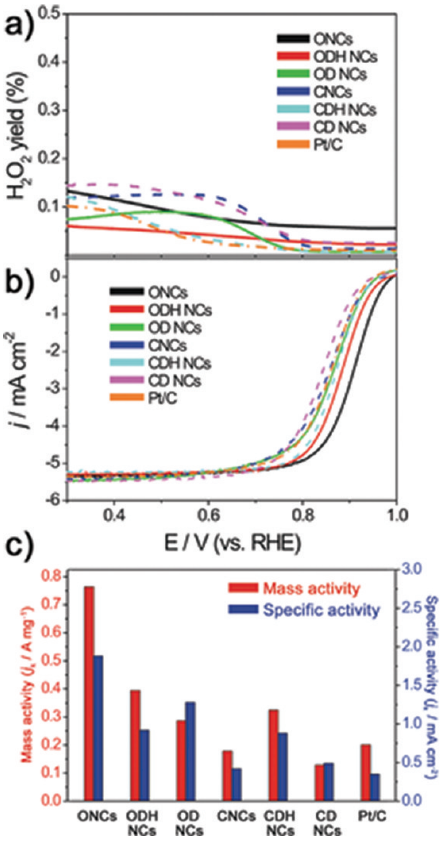

Figure 6. (a) H_2O_2 yield plots and (b) ORR polarization curves for the Pd–Pt bimetallic NCs and Pt/C obtained using a RRDE in O_2-saturated 0.1 M $HClO_4$ at scan rate of 10 mV s^{-1} and a rotation rate of 1600 rpm. The ring potential was held at 1.2 V *vs* RHE. The current densities were normalized to geometric surface area of the GC electrode (0.1256 cm^2). (c) Mass and area-specific activities at 0.85 V *vs* RHE for the various catalysts.

To decipher the formation mechanism of hollow structures, the shape evolution of the CDH NCs, as a representative example, was monitored by taking TEM images of the products sampled at different reaction times (Figure 5). Initially, Pt branches formed on the Pd NC seeds within 3 h through the deposition of Pt atoms, which were reduced by AA. After 3 h, small hollow interiors started to appear in the Pd seed regions. As the reaction proceeded, the hollow interior of the NCs gradually increased in size. Eventually, Pd–Pt nanostructures with dendritic branches and hollow interiors were produced. On the basis of these experimental results, we posited that the reduction of $PtCl_4^{2-}$ by AA produced Pt branches on the Pd NC surfaces at the beginning stage. After exhaustion of AA, simultaneous dissolution of Pd atoms and reduction of remaining $PtCl_4^{2-}$ were initiated by the galvanic replacement reaction, producing hollow interior in the Pd seed parts. Concomitantly, some amounts of dissolved Pd ($PdCl_4^{2-}$) were reduced onto the Pt branches. From this process, hollow Pd–Pt NCs with alloyed surfaces could be generated. To further confirm the proposed mechanism for the formation of Pd–Pt hollow structures, we tested the possibility of the preparation of CDH NCs by taking CD NCs and subjecting them to galvanic replacement in a decoupled step without AA. In fact, injection of the presynthesized CD NCs into a solution containing CTAC and K_2PtCl_4 successfully produced CDH NCs (Figure S5 in SI). Taken together, these findings show that manipulation of the degree of galvanic replacement is the key to the formation of various hollow structures.

The morphology-dependent electrocatalytic activities of various Pd–Pt bimetallic NCs toward ORR were investigated, and the results were compared with those of a commercial Pt/C catalyst (40 wt %, average Pt particle size = 3 nm). Cyclic voltammetry curves of Pd–Pt NCs obtained in 0.1 M $HClO_4$ exhibited distinct peaks associated with hydrogen adsorption and desorption, which were not significantly different from those of Pt/C (Figure S6 in SI). The electrochemically active surface areas (ECSA) for each NC were calculated by measuring the Coulombic charge for the desorption of the monolayer of hydrogen (Figure S6 in SI). The specific ECSA values for the ONCs, CNCs, ODH NCs, CDH NCs, OD NCs, CD NCs, and Pt/C were estimated to be 40.3, 42.3, 41.5, 39.8, 22.2, 25.9, and 57.7 $m^2\ g^{-1}$, respectively (Figure S7 in SI). Although the prepared Pd–Pt hollow NCs showed lower specific ECSA values than that of Pt/C due to their larger NC sizes, the hollow structures endowed ONCs, CNCs, ODH NCs, and CDH NCs with higher specific ECSA compared to OD and CD NCs. Panels a and b of Figure 6 display, respectively, H_2O_2 yield plots and ORR polarization curves for the prepared Pd–Pt bimetallic NCs and Pt/C obtained using a rotating ring disk electrode (RRDE), with a glassy carbon (GC) disk and a Pt ring, in O_2-saturated 0.1 M $HClO_4$. The ORR polarization curves obtained from disk currents were normalized to the geometric surface area of the GC electrode (0.1256 cm^2). The very low yields of H_2O_2 for all the catalysts (<0.15%), which were calculated from the ring current (see Methods section), imply high selectivity for four-electron reduction of oxygen.[43,44] The ORR polarization curves show that hollow structures generally have enhanced ORR activities as compared to Pd@Pt core–shell NCs. The ORR activities of the various Pd–Pt bimetallic NCs, estimated from the half-wave potential ($E_{1/2}$), follow the order ONCs > ODH NCs > CDH NCs > OD NCs > Pt/C > CNCs > CD NCs. To gain more insight into the different ORR activities, the kinetic current (j_k) associated with the intrinsic catalytic activity was obtained using a Koutecky–Levich plot for the ORR with various catalysts (see Methods section). At 0.85 V *versus* reversible hydrogen electrode (RHE), the ONCs exhibited a mass activity of 764.7 mA mg_{Pd+Pt}^{-1}, the highest value among the various catalysts and 1.9 and 3.8 times higher than those of the ODH NCs (393.9 mA mg_{Pd+Pt}^{-1}) and Pt/C (200.5 mA mg_{Pd+Pt}^{-1}), respectively (Figure 6c). The mass activities of the other catalysts are 324.4, 286.4, 178.1, and 128.5 mA mg_{Pd+Pt}^{-1} for the CDH NCs, OD NCs, CNCs, and CD NCs, respectively. The Pt mass activities (j_k, mA mg_{Pt}^{-1}) of the various NCs are also shown in Figure S8 in SI. Moreover, the area-specific activities of Pd–Pt NCs, obtained by normalization of j_k against ECSA, show a similar trend with mass activity (Figure 6c). Together with the most positive $E_{1/2}$ value (0.905 V *vs* RHE), these results signify that the ONCs drastically outperformed other Pd–Pt NCs and Pt/C. The accelerated durability tests further demonstrated that the ONCs have excellent electrochemical stability (Figure S9 in SI).

Through the electrocatalytic experiments, we found that the Pd–Pt NCs prepared from Pd octahedral NC templates exhibited higher ORR performances than the NCs from Pd cubic NC templates for each structure (ONCs *vs* CNCs, ODH NCs *vs* CDH NCs, and OD NCs *vs* CD NCs): ONCs, ODH NCs, and OD NCs had more positive $E_{1/2}$ values and showed, respectively, 4.3, 1.2, and 2.2 times higher mass activities than their counterparts prepared from Pd cubic NCs. Furthermore, the specific activities of Pd–Pt NCs produced by Pd octahedral NCs were higher than those of the NCs from Pd cubic NCs, irrespective of their structures (Figure 6c). These findings unambiguously reveal that the type of surface facet of NCs, which can be controlled by the morphology of sacrificial templates, plays a decisive role in determining the ORR activities of Pd–Pt NCs. Previous studies on the ORR in a $HClO_4$ solution have shown that {111} planes are more active than {100} planes.[45–47] For example, Zhang *et al.* have shown that mass and specific activity of Pt_3Ni octahedral NCs enclosed by {111} planes are, respectively, 2.8 and 4.0 times higher than those of Pt_3Ni cubic NCs enclosed by {100} planes.[46] Accordingly, the improved ORR activities of the ONCs, ODH NCs, and OD NCs compared to Pd–Pt NCs from the cubic Pd NC templates can be attributed to their {111} facet-dominant surfaces. On the other hand, of the NCs bound by the same surface facet, NCs with hollow structures exhibited enhanced mass activities toward ORR compared to the Pd@Pt core–shell NCs due to their larger specific ECSA: mass activities of the ONCs and ODH NCs were 2.67 and 1.38 times higher than that of the OD NCs, and CNCs and

CDH NCs showed 1.39 and 2.52 times higher mass activities than the CD NCs. The prominent ORR activity of the ONCs compared to ODH NCs can be ascribed to the relatively smooth surface feature of the ONCs compared to that of the ODH NCs. The amount of undercoordinated Pt atoms should be larger on the surface of ODH NCs than those on the ONCs due to their dendritic morphology. It is well-known that these active surface sites have higher oxygen binding energies, thus decrease the ORR activities of NCs.[11,48] However, unlike the case of the ONCs and ODH NCs, the CDH NCs showed better ORR activity than that of the CNCs. This can be understood by the observation that the {111} facets also developed to some extent in the branch tip regions of the CDH NCs, due to a release of strain imposed by the {100} facets at the interface (Figure S10 in SI).[49] A similar phenomenon was also observed in our previous work on Au@Pt heteronanostructures.[38] This finding further demonstrates that the type of surface facet is the most important parameter to determine the ORR activity of Pd–Pt NCs. In this regard, it is also noticeable that the OD NCs, which are enclosed by {111} facets, have higher mass and specific activities than those of the {100}-faceted CNCs, despite their lower specific ECSA compared to that of CNCs.

CONCLUSION

Pd–Pt bimetallic alloy NCs with hollow structures and dendritic Pd@Pt core–shell NCs could be selectively synthesized by a galvanic replacement method with Pd NCs with different morphologies as sacrificial templates. Fine control over the degree of galvanic replacement of Pd with Pt allowed the production of Pd–Pt NCs with distinctly different morphologies. The hollow NCs exhibited considerably enhanced oxygen reduction activities compared to those of Pd@Pt core–shell NCs, and their electrocatalytic activities were highly dependent on their morphologies. We found that the type of surface facet plays a crucial role in determining the ORR activities of Pd–Pt NCs. The Pd–Pt nanocages prepared from octahedral Pd NC templates exhibited the largest improvement in ORR performance. We expect that the present work will provide a promising strategy for the development of efficient ORR electrocatalysts and can also be extended to the preparation of other hybrid or hetero-nanostructures with desirable morphologies and functions.

METHODS

Chemicals and Materials. K_2PdCl_4 (Aldrich, 98%), K_2PdBr_4 (Aldrich, 98%), K_2PtCl_4 (Aldrich, 99.9%), L-ascorbic acid (Dae Jung Chemicals & Metals Co., 99.5%), cetyltrimethylammonium chloride (CTAC, Aldrich, solution in water, 25 wt %), $HClO_4$ (Aldrich, 60%), and Pt/C (Johnson Matthey, 40 wt %, average Pt particle size = 3 nm) were all used as received. Other chemicals, unless specified, were reagent grade, and high purified water with a resistivity of greater than 18.0 MΩ·cm was used in the preparation of aqueous solutions.

Preparation of Pd Octahedral and Cubic NCs. In a typical synthesis of Pd octahedral NCs, a 2 mL aqueous solution of K_2PdCl_4 (5 mM) and a 0.05 mL aqueous solution of L-ascorbic acid (50 mM) were injected to an aqueous solution of CTAC (10 mM, 7.95 mL) with gentle shaking, and then the resultant solution was heated at 90 °C for about 3 h in a conventional forced-convection drying oven. In a typical synthesis of Pd cubic NCs, an aqueous solution of CTAC (50 mM, 24 mL) was heated to 100 °C, and then 1 mL of L-ascorbic acid (300 mM) and 10 mL of K_2PdBr_4 (5 mM) were consequently added into the solution with vigorous stirring. The reaction was continued for 5 h at 100 °C with vigorous stirring.

Preparation of Pd–Pt Bimetallic NCs. In a typical synthesis of ONCs, 2 mL of Pd octahedral NC seed solution (1 mM_{Pd}) and 1 mL of K_2PtCl_4 (5 mM) were added to a 7 mL aqueous solution of CTAC (20 mM). The mixture was then heated to 100 °C and maintained at this temperature for 24 h with vigorous stirring. In a typical synthesis of ODH NCs, 2 mL of Pd octahedral NC seed solution (1 mM_{Pd}), 1 mL of K_2PtCl_4 (5 mM), and 0.5 mL of L-ascorbic acid (50 mM) were added to a 6.5 mL aqueous solution of CTAC (20 mM). The mixture was then heated to 100 °C and maintained at this temperature for 16 h with vigorous stirring. In a typical synthesis of OD NCs, 2 mL of Pd octahedral NC seed solution (1 mM_{Pd}), 1 mL of K_2PtCl_4 (5 mM), and 1 mL of L-ascorbic acid (100 mM) were added to a 6 mL aqueous solution of CTAC (20 mM). The mixture was then heated to 100 °C and maintained at this temperature for 3 h with vigorous stirring. For the synthesis of CNCs, CDH NCs, and CD NCs, Pd cubic NC seed solution (1 mM_{Pd}) instead of Pd octahedral NC seed solution was used under identical experimental conditions. The prepared Pd–Pt NCs were cleaned by repeated centrifugation of hydrosols at 9000 rpm for 8 min followed by redispersion of the NCs in deionized water to remove excess reagents.

Preparation of the Catalysts. The Ketjen Black carbon was used as a support for preparing the catalysts. First, the Ketjen Black carbon was dispersed in a high purified water. Then, a predetermined amount of the NCs was added to this dispersion. The resultant dispersion was sonicated for 2 h and then stirred for 24 h. The resulting dispersion was dried in a vacuum drying oven at 60 °C. The amounts of ONCs, CNCs, ODH NCs, CDH NCs, OD NCs, and CD NCs loaded on the Ketjen Black carbon determined by ICP-AES were 37.3, 42.8, 30.6, 45.4, 38.0, and 28.8 wt %, respectively.

Characterization of NCs. SEM images of the samples were taken using a field-emission scanning electron microscope (FESEM, Phillips Model XL30 S FEG). TEM, HRTEM, and HAADF-STEM characterizations were performed using a FEI Tecnai G2 F30 Super-Twin transmission electron microscope operated at 300 kV after placing a drop of hydrosol on carbon-coated Cu grids (200 mesh). The effective electron probe size and dwell time used in HAADF-STEM-EDS mapping experiments were 1.5 nm and 200 ms per pixel, respectively. The compositions of Pd–Pt bimetallic NCs were determined by ICP-AES (CIROS VISION). The surface compositions of Pd–Pt NCs were determined by Auger electron spectroscopy (Perkin-Elmer, SAM 4300). XRD patterns were obtained using a RIGAKU D/MAX-2500 diffractometer with Cu Kα (0.1542 nm) radiation. Electrochemical measurements were carried out in a three-electrode cell using a CH Instrument model 760D bipotentiostat. Pt wire and Ag/AgCl (in 3 M NaCl) were used as the counter and reference electrodes, respectively. All electrochemical data were obtained at room temperature, and all the potentials are reported with respect to the RHE. The electrolyte solutions were purged with high-purity N_2 gas before use for about 1 h. To prepare the working electrode, 10 μL of the catalyst dispersion (0.3 mg_{metal}/mL based on ICP-AES) was dropped onto a GC disk (diameter = 4 mm) of a RRDE with a Pt ring and dried at room temperature. The electrode was then washed several times with ethanol and water to remove stabilizing agents, and a thin layer of Nafion was placed on the catalyst-loaded GC electrode by dropping 15 μL of Nafion solution (0.05%). The dried working electrode was cleaned again by sequentially washing with ethanol and water and then electrochemically cleaned by 30 potential cycles between 0.1 and 1.3 V *versus* RHE at a scan rate of 50 mV s^{-1} to remove residual organic materials on the surface of the NCs. RRDE experiments were carried out using a rotator (ALS, RRDE-3A) in 0.1 M $HClO_4$ aqueous solution purged with O_2 prior to use for 30 min. The ring potential was held at 1.2 V *versus* RHE.[43] The specific kinetic current densities (j_k) associated with the intrinsic activity of the catalysts can be obtained by Koutecky–Levich eq (eq 1):[50]

$$1/j = 1/j_k + 1/j_d = 1/j_k + 1/B\omega^{1/2} \qquad (1)$$

where j_k is the kinetic current density, j_d is the diffusion-limited current density, ω is the angular frequency of rotation. The B parameter is defined as eq 2:

$$B = 0.62nFC_o D_o^{2/3} \upsilon^{-1/6} \qquad (2)$$

where n is the overall number of electrons, F is the Faraday constant (96485 C mol^{-1}), C_o is the concentration of molecular oxygen in the electrolyte (1.26×10^{-6} mol cm^{-3}), D_o is the diffusion coefficient of the molecular O_2 in 0.1 M $HClO_4$ solution (1.93×10^{-5} cm^2 s^{-1}), and υ is the viscosity of the electrolyte (1.009×10^{-2} cm^2 s^{-1}).[10] The yield of H_2O_2 was calculated by the following equation (eq 3):[43]

$$\text{yield of } H_2O_2\ (\%) = 200 \times (I_r/N)/((I_d + I_r)/N) \qquad (3)$$

where I_r is ring current, I_d is disk current, and N is current collection efficiency of the Pt ring. N was experimentally determined to be 0.35 from the reduction of $K_3Fe[CN]_6$.

Conflict of Interest: The authors declare no competing financial interest.

Acknowledgment. This work was supported by Basic Science Research Programs (2010-0029149), EPB Center (2008-0062042), Future-based Technology Development Program (Nano Fields) (2009-0082640), and WCU Program (R31-2008-000-10071-0) through the National Research Foundation (NRF) funded by the Korean government (MEST).

Supporting Information Available: Experimental details and additional figures. This material is available free of charge *via* the Internet at http://pubs.acs.org.

REFERENCES AND NOTES

1. Stamenkovic, V. R.; Mun, B. S.; Arenz, M.; Mayrhofer, J. J.; Lucas, C. A.; Wang, G.; Ross, P. N.; Markovic, N. M. Trends in Electrocatalysis on Extended and Nanoscale Pt-Bimetallic Alloy. *Nat. Mater.* **2008**, *6*, 241–247.
2. Greeley, J.; Stephens, I. E. L.; Bondarenko, A. S.; Johansson, T. P.; Hansen, H. A.; Jaramillo, T. F.; Rossmeisl, J.; Chorkendorff, I.; Nørskov, J. K. Alloys of Platinum and Early Transition Metals as Oxygen Reduction Electrocatalysts. *Nat. Chem.* **2009**, *1*, 552–556.
3. Kang, Y.; Murray, C. B. Synthesis and Electrocatalytic Properties of Cubic Mn–Pt Nanocrystals (Nanocubes). *J. Am. Chem. Soc.* **2010**, *132*, 7568–7569.
4. Mazumder, V.; Lee, Y.; Sun, S. Recent Development of Active Nanoparticle Catalysts for Fuel Cell Reactions. *Adv. Funct. Mater.* **2010**, *20*, 1224–1231.
5. Koenigsmann, C.; Santulli, A. C.; Gong, K.; Vukmirovic, M. B.; Zhou, W.-P.; Sutter, E.; Wong, S. S.; Adzic, R. R. Enhanced Electrocatalytic Performance of Processed, Ultrathin, Supported Pd–Pt Core–Shell Nanowire Catalysts for the Oxygen Reduction Reaction. *J. Am. Chem. Soc.* **2011**, *133*, 9783–9795.
6. Liu, L.; Pippel, E. Low-Platinum-Content Quaternary PtCuCoNi Nanotubes with Markedly Enhanced Oxygen Reduction Activity. *Angew. Chem., Int. Ed.* **2011**, *50*, 2729–2733.
7. Adzic, R. R.; Zhang, J.; Sasaki, K.; Vukmirovic, M. B.; Shao, M.; Wang, J. X.; Nilekar, A. U.; Mavrikakis, M.; Valerio, J. A.; Uribe, F. Platinum Monolayer Fuel Cell Electrocatalysts. *Top. Catal.* **2007**, *46*, 249–262.
8. Steele, B. C. H.; Heinzel, A. Materials for Fuel-Cell Technologies. *Nature* **2001**, *414*, 345–352.
9. Koenigsmann, C.; Zhou, W.-P.; Adzic, R. R.; Sutter, E.; Wong, S. S. Size-Dependent Enhancement of Electrocatalytic Performance in Relatively Defect-Free, Processed Ultrathin Platinum Nanowires. *Nano Lett.* **2010**, *10*, 2806–2811.
10. Wang, C.; Daimon, H.; Onodera, T.; Koda, T.; Sun, S. A General Approach to the Size- and Shape-Controlled Synthesis of Platinum Nanoparticles and Their Catalytic Reduction of Oxygen. *Angew. Chem., Int. Ed.* **2008**, *47*, 3588–3591.
11. Wang, J. X.; Ma, C.; Choi, Y.; Su, D.; Zhu, Y.; Liu, P.; Si, R.; Vukmirovic, M. B.; Zhang, Y.; Adzic, R. R. Kirkendall Effect and Lattice Contraction in Nanocatalysts: A New Strategy To Enhance Sustainable Activity. *J. Am. Chem. Soc.* **2011**, *133*, 13551–13557.
12. Atacee-Esfahani, H.; Nemoto, Y.; Wang, L.; Yamauchi, Y. Rational Synthesis of Pt Spheres with Hollow Interior and Nanosponge Shell Using Silica Particles as Template. *Chem. Commun.* **2011**, *47*, 3885–3887.
13. Chen, Z.; Waje, M.; Li, W.; Yan, Y. Supportless Pt and PtPd Nanotubes as Electrocatalysts for Oxygen-Reduction Reactions. *Angew. Chem., Int. Ed.* **2007**, *46*, 4060–4063.
14. Wang, L.; Yamauchi, Y. Controlled Aqueous Solution Synthesis of Platinum–Palladium Alloy Nanodendrites with Various Compositions Using Amphiphilic Triblock Copolymers. *Chem. Asian J.* **2010**, *5*, 2493–2498.
15. Choi, S.-I.; Choi, R.; Han, S. W; Park, J. T. Synthesis and Characterization of Pt_9Co Nanocubes with High Activity for Oxygen Reduction. *Chem. Commun.* **2010**, *46*, 4950–4952.
16. Choi, S.-I.; Choi, R.; Han, S. W; Park, J. T. Shape-Controlled Synthesis of Pt_3Co Nanocrystals with High Electrocatalytic Activity toward Oxygen Reduction. *Chem.—Eur. J.* **2011**, *17*, 12280–12284.
17. Wu, J.; Zhang, J.; Peng, Z.; Yang, S.; Wagner, F. T.; Yang, H. Truncated Octahedral Pt_3Ni Oxygen Reduction Reaction Electrocatalysts. *J. Am. Chem. Soc.* **2010**, *132*, 4984–4985.
18. Kim, J.; Lee, Y.; Sun, S. Structurally Ordered FePt Nanoparticles and Their Enhanced Catalysis for Oxygen Reduction Reaction. *J. Am. Chem. Soc.* **2010**, *132*, 4996–4997.
19. Fang, Y.-H.; Liu, Z.-P. Mechanism of Oxygen Electro-Reduction on Au-Modified Pt: Minimizing O Coverage and Pt Site Exposure toward Highly Stable and Active Cathode. *J. Phys. Chem. C* **2011**, *115*, 17508–17515.
20. Atacee-Esfahani, H.; Wang, L.; Nemoto, Y.; Yamauchi, Y. Synthesis of Bimetallic Au@Pt Nanoparticles with Au Core and Nanostructured Pt Shell toward Highly Active Electrocatalysts. *Chem. Mater.* **2010**, *22*, 6310–6318.
21. Atacee-Esfahani, H.; Wang, L.; Yamauchi, Y. Block Copolymer Assisted Synthesis of Bimetallic Colloids with Au Core and Nanodendritic Pt Shell. *Chem. Commun.* **2010**, *46*, 3684–3686.
22. Liu, Z.; Koh, S.; Yu, C.; Strasser, P. Synthesis, Dealloying, and ORR Electrocatalysis of PDDA-Stabilized Cu-Rich Pt Alloy Nanoparticles. *J. Electrochem. Soc.* **2007**, *154*, B1192–B1199.
23. Gong, K.; Su, D.; Adzic, R. R. Platinum-Monolayer Shell on $AuNi_{0.5}Fe$ Nanoparticle Core Electrocatalyst with High Activity and Stability for the Oxygen Reduction Reaction. *J. Am. Chem. Soc.* **2010**, *132*, 14364–14366.
24. Lim, B.; Jiang, M.; Camargo, P. H. C.; Cho, E. C.; Tao, J.; Lu, X.; Zhu, Y.; Xia, Y. Pd–Pt Bimetallic Nanodendrites with High Activity for Oxygen Reduction. *Science* **2009**, *324*, 1302–1305.
25. Zhang, H.; Yin, Y.; Hu, Y.; Li, C.; Wu, P.; Wei, S.; Cai, C. Pd@Pt Core–Shell Nanostructures with Controllable Composition Synthesized by a Microwave Method and Their Enhanced Electrocatalytic Activity toward Oxygen Reduction and

Methanol Oxidation. *J. Phys. Chem. C* **2010**, *114*, 11861–11867.

26. Sasaki, K.; Naohara, H.; Cai, Y.; Choi, Y. M.; Liu, P.; Vukmirovic, M. B.; Wang, J. X.; Adzic, R. R. Core-Protected Platinum Monolayer Shell High-Stability Electrocatalysts for Fuel-Cell Cathodes. *Angew. Chem., Int. Ed.* **2010**, *49*, 8602–8607.
27. An, K.; Hyeon, T. Synthesis and Biomedical Applications of Hollow Nanostructures. *Nano Today* **2009**, *4*, 359–373.
28. Mahmoud, M. A.; Saira, F.; El-Sayed, M. A. Experimental Evidence for the Nanocage Effect in Catalysis with Hollow Nanoparticles. *Nano Lett.* **2010**, *10*, 3764–3769.
29. Cho, E. C.; Camargo, P. H. C.; Xia, Y. Synthesis and Characterization of Noble-Metal Nanostructures Containing Gold Nanorods in the Center. *Adv. Mater.* **2010**, *22*, 744–748.
30. Peng, Z.; Wu, J.; Yang, H. Synthesis and Oxygen Reduction Electrocatalytic Property of Platinum Hollow and Platinum-on-Silver Nanoparticles. *Chem. Mater.* **2010**, *22*, 1098–1106.
31. Chen, H. M.; Liu, R. S.; Lo, M. Y.; Chang, S. C.; Tsai, L. D.; Peng, Y. M.; Lee, J. F. Hollow Platinum Spheres with Nano-Channels: Synthesis and Enhanced Catalysis for Oxygen Reduction. *J. Phys. Chem. C* **2008**, *112*, 7522–7526.
32. Zhang, H.; Jin, M.; Wang, J.; Kim, M. J.; Yang, D.; Xia, Y. Nanocrystals Composed of Alternating Shells of Pd and Pt Can Be Obtained by Sequentially Adding Different Precursors. *J. Am. Chem. Soc.* **2011**, *133*, 10422–10425.
33. Yuan, Q.; Zhou, Z.; Zhuanga, J.; Wang, X. Pd−Pt Random Alloy Nanocubes with Tunable Compositions and Their Enhanced Electrocatalytic Activities. *Chem. Commun.* **2010**, *46*, 1491–1493.
34. Habas, S.; Lee, H.; Radmilovic, V.; Somorjai, G. A.; Yang, P. Shaping Binary Metal Nanocrystals through Epitaxial Seeded Growth. *Nat. Mater.* **2007**, *6*, 692–697.
35. Lee, H.; Habas, S. E.; Somorjai, G. A.; Yang, P. Localized Pd Overgrowth on Cubic Pt Nanocrystals for Enhanced Electrocatalytic Oxidation of Formic Acid. *J. Am. Chem. Soc.* **2008**, *130*, 5406–5407.
36. *CRC Handbook of Chemistry and Physics*, 84th ed.; Lide, D. R., Ed.; CRC Press: Boca Raton, FL, 2004.
37. Min, M.; Kim, C.; Yang, Y. I.; Yi, J.; Lee, H. Surface-Specific Overgrowth of Platinum on Shaped Gold Nanocrystals. *Phys. Chem. Chem. Phys.* **2009**, *11*, 9759–9765.
38. Kim, Y.; Hong, J. W.; Lee, Y. W.; Kim, M.; Kim, D.; Yun, W. S.; Han, S. W. Synthesis of AuPt Heteronanostructures with Enhanced Electrocatalytic Activity toward Oxygen Reduction. *Angew. Chem., Int. Ed.* **2010**, *49*, 10197–10201.
39. Sun, Y.; Wiley, B.; Li, Z.-Y.; Xia, Y. Synthesis and Optical Properties of Nanorattles and Multiple-Walled Nanoshells/Nanotubes Made of Metal Alloys. *J. Am. Chem. Soc.* **2004**, *126*, 9399–9406.
40. Khalavka, Y.; Becker, J.; Sönnichsen, C. Synthesis of Rod-Shaped Gold Nanorattles with Improved Plasmon Sensitivity and Catalytic Activity. *J. Am. Chem. Soc.* **2008**, *131*, 1871–1875.
41. He, W.; Wu, X.; Liu, J.; Hu, X.; Zhang, K.; Hou, S.; Zhou, W.; Xie, S. Design of AgM Bimetallic Alloy Nanostructures (M = Au, Pd, Pt) with Tunable Morphology and Peroxidase-like Activity. *Chem. Mater.* **2010**, *22*, 2988–2994.
42. Zhang, H.; Jin, M.; Liu, H.; Wang, J.; Kim, M. J.; Yang, D.; Xie, Z.; Liu, J.; Xia, Y. Facile Synthesis of Pd−Pt Alloy Nanocages and Their Enhanced Performance for Preferential Oxidation of CO in Excess Hydrogen. *ACS Nano* **2011**, *5*, 8212–8222.
43. Wu, G.; More, K. L.; Johnston, C. M.; Zelenay, P. High-Performance Electrocatalysts for Oxygen Reduction Derived from Polyaniline, Iron, and Cobalt. *Science* **2011**, *332*, 433–447.
44. Liang, Y.; Li, Y.; Wang, H.; Zhou, J.; Wang, J.; Regier, T.; Dai, H. Co_3O_4 Nanocrystals on Graphene as a Synergistic Catalyst for Oxygen Reduction Reaction. *Nat. Mater.* **2010**, *10*, 780–786.
45. Stamenkovic, V. R.; Fowler, B.; Mun, B. S.; Wang, G.; Ross, P. N.; Lucas, C. A.; Markovic, N. M. Improved Oxygen Reduction Activity on $Pt_3Ni(111)$ *via* Increased Surface Site Availability. *Science* **2007**, *315*, 493–497.
46. Zhang, J.; Yang, H.; Fang, J.; Zou, S. Synthesis and Oxygen Reduction Activity of Shape-Controlled Pt_3Ni Nanopolyhedra. *Nano Lett.* **2010**, *10*, 638–644.
47. Sánchez-Sánchez, C. M.; Solla-Gullón, J.; Vidal-Iglesias, F. J.; Aldaz, A.; Montiel, V.; Herrero, E. Imaging Structure Sensitive Catalysis on Different Shape-Controlled Platinum Nanoparticles. *J. Am. Chem. Soc.* **2010**, *132*, 5622–5624.
48. Shao, M.; Peles, A.; Shoemaker, K. Electrocatalysis on Platinum Nanoparticles: Particle Size Effect on Oxygen Reduction Reaction Activity. *Nano Lett.* **2011**, *11*, 3714–3719.
49. Peng, Z.; Yang, H. Designer Platinum Nanoparticles: Control of Shape, Composition in Alloy, Nanostructure and Electrocatalytic Property. *Nano Today* **2009**, *4*, 143–164.
50. Bard, A. J.; Faulkner, L. R. *Electrochemical Methods: Fundamentals and Applications*; Wiley: New York, 2000.